Cell Reports
Physical Science

CellPress
OPEN ACCESS

Article

Prevention of lithium-ion battery thermal runaway using polymer-substrate current collectors

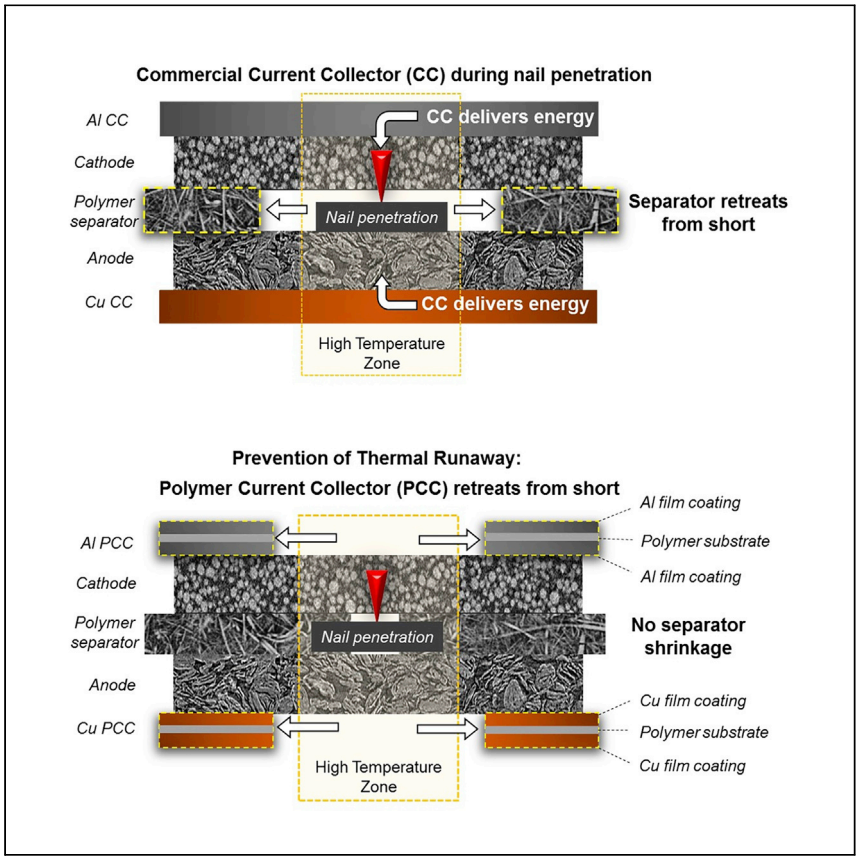

Most instances of thermal runaway in lithium-ion batteries stem from an internal short circuit. One approach to reducing risk of thermal runaway is isolation of internal short circuits as soon as they occur. Pham et al. describe a current collector that consists of metal coated onto a polymer substrate that can isolate internal short circuits and consistently prevent thermal runaway during mechanical abuse.

Martin T.M. Pham, John J. Darst, William Q. Walker, ..., Eric Darcy, Donal P. Finegan, Paul R. Shearing

donal.finegan@nrel.gov (D.P.F.)
p.shearing@ucl.ac.uk (P.R.S.)

HIGHLIGHTS

Polymer current collectors prevented thermal runaway in Li-ion 18650 cells abuse

Operando high-speed X-ray radiography evaluation of nail-penetration abuse experiments

Post-mortem 3D X-ray CT has been applied for visual analysis of the cells after abuse

The mechanism of short-circuit isolation in novel current collectors has been explained

Pham et al., Cell Reports Physical Science 2, 100360
March 24, 2021 © 2021
https://doi.org/10.1016/j.xcrp.2021.100360

Cell Reports
Physical Science

CellPress
OPEN ACCESS

Article

Prevention of lithium-ion battery thermal runaway using polymer-substrate current collectors

Martin T.M. Pham,[1] John J. Darst,[2] William Q. Walker,[2] Thomas M.M. Heenan,[1,3] Drasti Patel,[1] Francesco Iacoviello,[1] Alexander Rack,[4] Margie P. Olbinado,[4] Gareth Hinds,[5] Dan J.L. Brett,[1,3] Eric Darcy,[2] Donal P. Finegan,[6,*] and Paul R. Shearing[1,3,7,*]

SUMMARY

Isolating electronically conducting material from internal short circuits is a promising way to prevent the onset of thermal runaway within lithium-ion cells. Here, a metal-coated polymer current collector, which is designed to disconnect internal short circuits by withdrawing from the heating region, is tested in 18650 cells. In addition to having lower mass and manufacturing costs, cells with metal-coated polymer current collectors demonstrate a reduced risk of thermal runaway during nail penetration. High-speed synchrotron X-ray radiography of 18650 cells during nail-penetration testing, in tandem with pre- and post-mortem X-ray computed tomography, provides insights into the function of the current collectors. The results are compared with those of 18650 cells with standard commercial aluminum and copper current collectors. Cells with aluminum-coated polymer current collectors demonstrated 100% success in thermal runaway prevention during nail penetration, retaining a cell voltage >4.00 V, while standard cells consistently experienced thermal runaway.

INTRODUCTION

Lithium (Li)-ion batteries have been the cornerstone of energy storage systems in the thriving development of modern consumer electronics. Furthermore, high-energy density cells of the 18650 format can exceed 3 Ah, for which myriad applications exist in aerospace and electric vehicles (EVs) with varying high-energy and high-power demands.[1–3] However, the hazardous nature of Li-ion batteries undergoing thermal runaway,[4–6] particularly in cases of mechanically induced failure,[6] have intensified the scrutiny of the safety of Li-ion batteries for consumer applications.

The role of the current collector (CC) in a cell is to provide an electronic conduction pathway to the anode and cathode; metals such as aluminum and copper are typically used as they are electrochemically stable across the respective operating potential windows of the cathode and anode, thus preventing degradation.[7,8] Relatively high thicknesses are used for conventional CCs to avoid tearing of the material during roll-to-roll manufacture, which negatively affects the energy density of cells. Conventional CCs can carry large currents and are thus a critical component for sustaining internal short circuits that can lead to thermal runaway. The sequence of precursor events indicative of widespread thermal runaway has been widely investigated[9–13] and reviewed[4,14–16] through the use of multiple direct and indirect techniques.[17–25] During nail penetration of an 18650 cell, internal cell temperatures >800°C[26] and surface temperatures >600°C are common[27–30] due to the ~70 kJ

[1]Electrochemical Innovation Laboratory, Department of Chemical Engineering, University College London, London WC1E 7JE, UK

[2]NASA Johnson Space Center, 2101 East NASA Parkway, Houston, TX 77058, USA

[3]The Faraday Institution, Quad One, Harwell Science and Innovation Campus, Didcot OX11 0RA, UK

[4]The European Synchrotron (ESRF), 71 Avenue des Martyrs, 38000 Grenoble, France

[5]National Physical Laboratory, Hampton Road, Teddington, London TW11 0LW, UK

[6]National Renewable Energy Laboratory, 15013 Denver West Parkway, Golden, CO 80401, USA

[7]Lead contact

*Correspondence:
donal.finegan@nrel.gov (D.P.F.),
p.shearing@ucl.ac.uk (P.R.S.)

https://doi.org/10.1016/j.xcrp.2021.100360

This is an open access article under the CC BY-NC-ND license (http://creativecommons.org/licenses/by-nc-nd/4.0/).

of heat[18] that is typically produced. In EV battery packs, in which it is common for powertrains to consist of thousands of 18650 cells,[31] measures are taken to eliminate or at least minimize the risk of failure. Common failure modes and means to prevent failure have been reviewed in-depth,[6,32–37] but little change has ever been made to the architecture of CCs for improved battery safety commercially. Recently reported re-engineering of the CC to improve battery safety by Naguib et al.[38] restructured the electrode and CC design to produce impact-tolerant "slitted" construction that could withstand mechanical impact and by Liu et al.,[39] using a positive temperature coefficient (PTC) material within a CC configuration to isolate the region of short circuit from the rest of the battery. It is notable that connection of the two most electrically conductive materials within a cell (the CCs) leads to the most severe internal short circuit, thus one of the most probable conditions for thermal runaway to occur. Therefore, removal or isolation of the CC during an internal short circuit holds great promise for significantly reducing the risk of thermal runaway initiating and propagating through the cell.

In this work, the prevention of thermal runaway using metal-coated polymer substrate CCs (PCCs) within 18650 cells are investigated and compared with 18650 cells with standard conventional metallic CCs. Direct visualization of the function of the PCC in preventing thermal runaway during nail-penetration testing is evaluated with high-speed X-ray radiography and post-mortem computed tomography (CT).[26–29,40] We anticipate that this work may have a significant impact across the battery community, providing increased confidence in the manufacture of inherently safer batteries with PCCs, without compromising the performance of the cell, as the PCC increases cell gravimetric energy density and reduces material costs compared to conventional CCs.

RESULTS

Prevention of thermal runaway and fractional thermal runaway calorimetry (FTRC) data

The nail-penetration process for cells with a conventional metal foil CC and those with PCCs is illustrated schematically in Figures 1A and 1B, respectively. In the conventional metal foil CC cell, the short circuit is maintained between adjacent electrode layers by the presence of the nail, leading to continuous heat generation and eventually thermal runaway. The principle of the PCC safety mechanism is that the initial heat generation caused by the short circuit causes thermal degradation and thus the PCC periphery to shrink away from the nail, breaking the short circuit and preventing thermal runaway.

A variety of cell configurations were used to provide a basis for comparison of the Al PCC and Cu PCC and are grouped into 4 categories—G1 (Al PCC, Cu CC), G2 (Cu PCC, Al CC), G3 (Al + Cu PCC), and G4 (Al + Cu CC)—as shown in Figure 1C. Therefore, comparison of G1 with G4 (and G2 with G3) provided insights into the effectiveness of the Al PCC in preventing thermal runaway. Similarly, evaluation of the Cu PCCs could be made by comparison of G2 with G4 (and G1 with G3). Lastly, both PCCs together could be evaluated via comparison between G3 and G4.

Tomograms of the fresh cells, acquired at a 10 μm voxel resolution (Figure 1C), allowed us to identify and resolve the commercial CCs within the 18650 cells (G1, G4). However, as the metal film coatings on the PCCs were ~0.5 μm thick (G2, G3), they were not sufficiently resolved and were not apparent in the ortho-slices shown, thus leading to the contrasting cylindrical ortho-slices between the cell groups (Figure 1C). Mass differences between the commercial CCs and the PCCs

CellPress
OPEN ACCESS

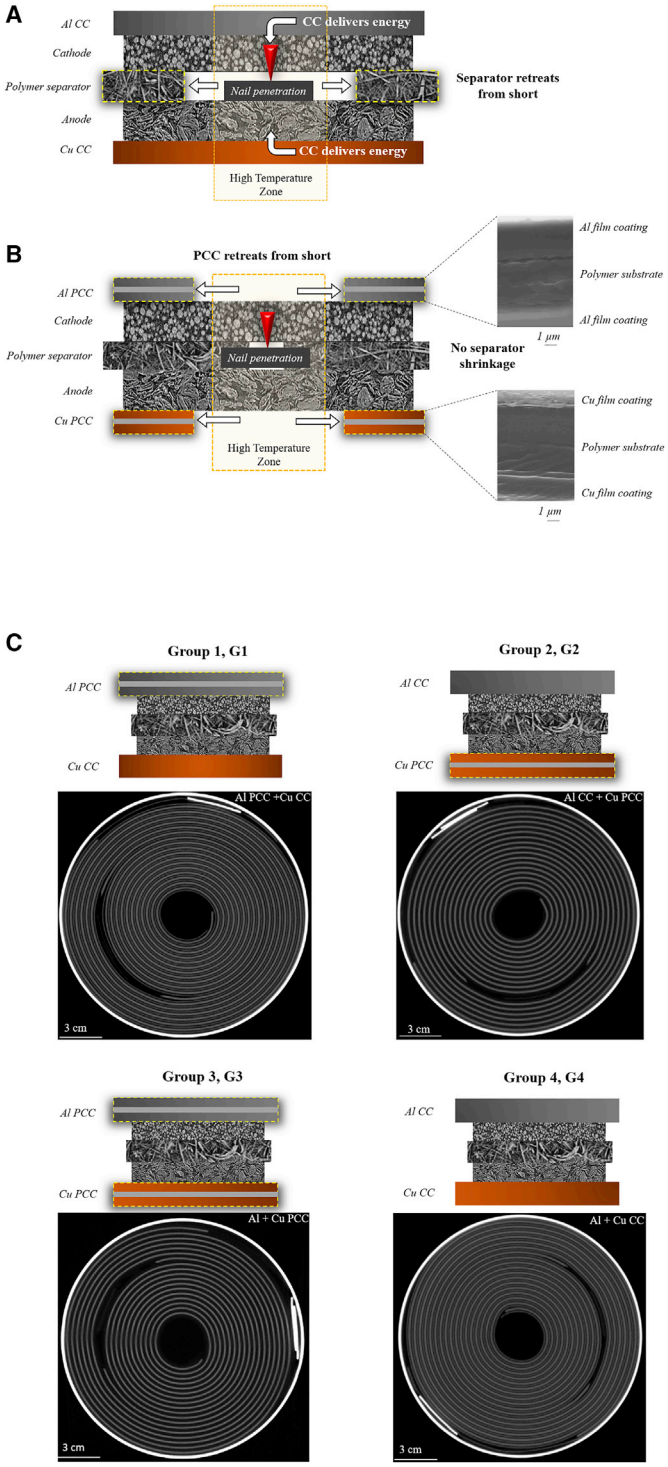

Figure 1. Nail penetration and failure mechanism

(A) Nail penetration of a standard commercial metal CC cell.

(B) Failure mitigation mechanism of Al PCC and Cu PCC cell during nail penetration; SEM insets of the PCC cross-sections illustrate the ~8 μm polymer substrate "core" and ~0.5 μm metal film coating. See supplemental experimental procedures for details of the SEM analysis.

(C) Cell specifications of CCs used in this work. Cells are manufactured with one or both PCCs, with G4 used as the standard commercial control group. Cylindrical cross-section ortho-slices are shown with the corresponding cell group. Tomograms were acquired at 10 μm pixel size for each cell group.

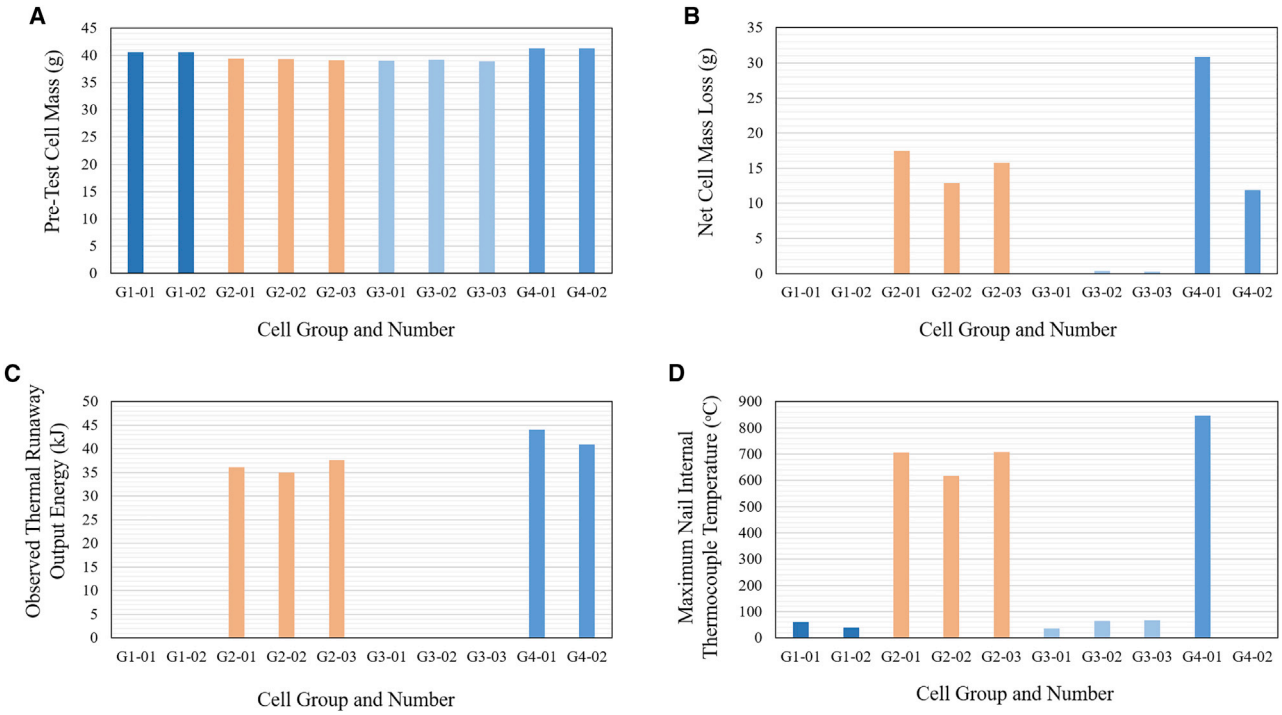

Figure 2. Failure tests

For each CC configuration in the 4 cell groups, multiple failure tests were conducted. Repeated tests of cell group 1 are denoted as G1-0#.

(A) Pre-nail penetration test mass of each cell.

(B) Cell mass loss after the nail penetration tests.

(C) Calculated thermal runaway calorific output derived from the fractional thermal runaway calorimeter.

(D) Maximum temperature measured by the thermocouple within the tip of the nail. Please note that for the G4-02 cell, the thermocouple within the nail failed, and no temperature was recorded for this test.

are shown in Figure S1. A significant reduction in cell mass was observed, and further analysis on gravimetric energy density increase due to the PCCs can be found in Note S1.

FTRC and analysis of the thermal data provided by thermocouple instrumentation facilitated analysis of the impact of nail penetration, with concurrent visualization provided by high-speed X-ray radiography. Further details of the experiment can be found in the Experimental Methods.

In the nail-penetration tests conducted with FTRC and reported in this work, thermal runaway was not observed in any of the cells that contained the Al PCC (G1 and G3). This was supported by a comparison of mass loss (Figure 2B), calorific output (Figure 2C), and maximum nail tip temperature (Figure 2D) for cells that contained the Al PCC and those that did not. In contrast, thermal runaway was initiated in cells that contained only the Cu PCC (G2) and in the cells with only standard commercial metallic CCs (G4). The Cu PCC is examined further in Figure S2 and Note S2.

As the CC provides an electrical pathway for the micro-short circuit, the greatest elevated temperature will be experienced by the CC due to Ohmic heating before dissipating heat to the adjacent electrodes and then the separator. Therefore, in instances with the PCC, the PCC will experience a higher temperature than the separator, and thus thermal degradation of the PCC will occur first.

CellPress
OPEN ACCESS

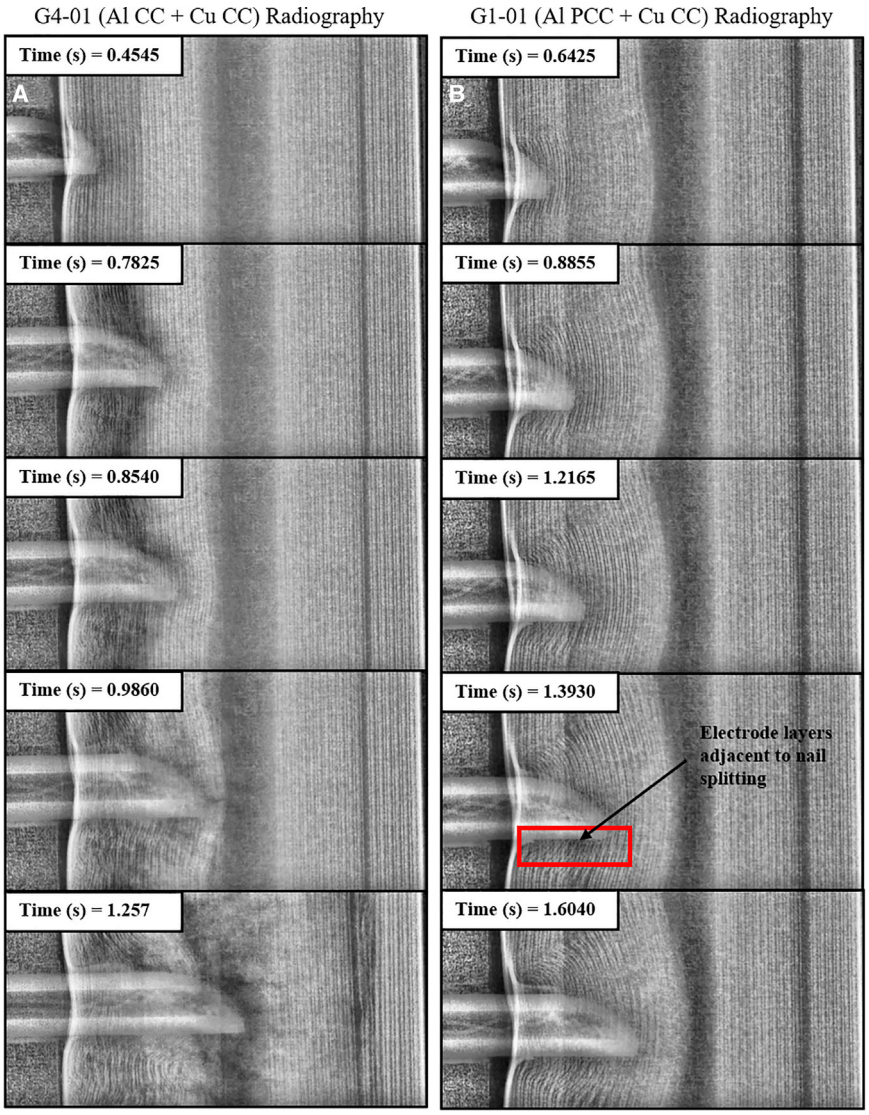

Figure 3. Radiography of cells undergoing nail penetration

Penetration continues up to a depth of 9 mm, or until the nail fails to penetrate further. Time stamps are shown in the top left of each frame.

(A) G4-01 (standard commercial Al CC + standard commercial Cu CC)–the onset of thermal runaway occurs immediately upon penetration, and in the fourth frame, cracking of the electrode assembly is evident.

(B) G1-01 (Al PCC + standard commercial Cu CC)–complete absence of thermal runaway and clear shear stress exerted on the cylindrical electrode assembly. Videos of each of these tests are provided as Videos S1 and S2.

Operando synchrotron radiography of nail-penetration experiments

Different materials and phases were identifiable during *operando* X-ray radiography. In the central core, typically filled with weakly attenuating electrolyte, gases and materials with different contrast were observed to flow upward, providing indicators of thermal decomposition of electrolyte and of the active materials in the electrode assembly. These observations were further reinforced by evidence of electrode disintegration and upward flow of electrode layers.

In Figure 3A, various stages of the nail penetration of cell G4-01 (standard commercial Al CC + Cu CC; Video S1) are shown. At 0.4545 s, as the nail penetrated the cell wall and began to impinge on the structure of the cylindrical electrode assembly, the

initial bend in the electrode layer was followed by a firm spring back into position as the nail proceeded to the next layer. In this radiography frame, after the nail had penetrated through the outer four electrode layers, the first two layers had sprung back into position and were already showing signs of splitting and thermal degradation. These sites acted as nucleation points for thermal runaway via micro- and later macro-short circuiting.

As the macro-short circuiting of the nail-penetrated electrode layers occurred, electrolyte and active material decomposition led to macroscopic gas generation, which resulted in the flow of material toward the cell cap before cell rupture. At 0.7825 s in Figure 3A, thermal runaway had initiated in the previously penetrated layers, and fluidization of these layers was observed. Penetration continued into the inner half of the cylindrical electrode assembly, shown at 0.8540 s in Figure 3A; thermal degradation observed in the form of electrode disintegration around the nail was also initiated locally and later propagated to widespread thermal runaway at 0.9860 s. At the tip of the nail at 0.9860 s, the inner electrode layers were seen to be cracking horizontally. At 1.257 s in Figure 3A, widespread thermal runaway on the other side of the cell was observed. The mechanism of thermal runaway observed in Figure 3A for cell G4-01 was consistent with that for cell G4-02. The dynamic process is illustrated in Video S1.

In Figure 3B, corresponding stages of the nail penetration of cell G1-01 (Al PCC + Cu CC; Video S2) are shown. The characteristic behavior during nail penetration contrasted greatly with cell G4-01, with a significantly more ductile response of the electrode assembly to the penetration of the nail and very little evidence of electrolyte decomposition or widespread fracture of electrode layers. As the first 5 electrode layers were penetrated at 0.6425 s, the shear stress imposed by the nail on the electrode assembly caused the material to shift. This force can be observed by the deformed electrode assembly layers adjacent to the nail. This cumulative displacement of electrode layers resulted in the curvature of the internal layers of the electrode assembly into the central core region. However, in contrast to the behavior observed for cell G4-01, local heat generation was evidently rapidly curtailed by shrinkage of the Al PCC from the nail, and all of the layers remained largely intact despite the significant curvature.

Some localized damage was evident close to the surface of the nail, where the electrode assembly was observed to have split (highlighted at 1.3930 s in Figure 3B); this was especially visible along the bottom edge of the nail. From 1.2165 s to 1.6040 s, in Figure 3B, the shear stress that affected the electrode layers caused further deformation of the layers and displacement of the electrode assembly in the central core of the cell. Further splitting of the tips of the electrode assembly in contact with the penetrating nail was observed, with a maximum temperature of 61.4°C recorded. This temperature was measured by a thermocouple at the tip of the nail; thus, it was lower than the actual temperature of the PCC. However, the temperature experienced was much lower than the melting point of the polymer substrate; this provided further evidence of the hypothesized shrinkage of the PCC at the periphery where the nail had penetrated, rather than melting of the PCC.

The rigid spring back of electrode layers observed in cell G4-01 was not evident for cell G1-01. This more ductile response was likely to be a result of the elongation property of the PCC shown in Figure S1. In addition, the interruption of the thermal breakdown of the material local to the surface of the nail maintained the integrity of

CellPress
OPEN ACCESS

the electrode assembly, allowing it to deform plastically as penetration progressed. Further analysis of these findings was provided by the post-mortem CT in Figure 4.

No thermal runaway of cell G1-01 occurred after waiting 10 min with the nail inside the cell. Subsequent removal and voltage measurement revealed an open circuit voltage (OCV) of 4.077 V for G1-01. After 8 months, the OCV of the cell was measured as ~3.60 V, which demonstrated a highly effective isolation of electrically conducting paths between the punctured electrode layers.

From these tests on the Al CC + Cu CC (G4 cells) and the Al PCC + Cu CC (G1 cells), primary indicators of the safety mechanisms of the Al PCC could be observed. The prevention of thermal runaway can be attributed to the Al PCC providing electrical isolation of the cathode and the nail (which is electrically connected to the anode via the cell can and the Cu CC). Because of the temperature sensed by the nail thermocouple, it could be ascertained that the polypropylene separator had not failed and that the Al PCC had indeed operated with the hypothesized shrinking mechanism, as detailed in Figure 1B. This was due to the initial micro-short circuit, which occurred as the nail penetrated the cell and came into contact with the Al PCC and the cathode; this "soft" short circuit caused an initial surge of current to the local area, which caused elevated local temperatures, as measured by the thermocouple at the tip of the nail. As the temperature increased to ~60°C, the Al PCC polymer core began to experience thermal damage and shrink from the nail, which was observed as a frayed electrode assembly adjacent to the nail tip (highlighted at 1.3930 s in Figure 3B). As a result, the Al film coating on either side of the PCC lost electrical contact with the nail as it also retreated with the polymer core of the Al PCC. This is in stark contrast to the mechanisms observed in Figure 3A for standard commercial cells, whereby the Al CC did not retreat and remained electrically connected. This enabled a continuous positive feedback between cell short circuit and temperature elevation, which resulted in separator failure before thermal runaway.

Cells with the Al PCC did not undergo thermal runaway, as the PCC isolated the cathode from the nail by polymer shrinkage as the temperature increased. However, because the penetrating nail was in continuous contact with the negative steel cell casing, the Cu PCC was ineffective in preventing thermal runaway in the absence of the Al PCC. Further work in other cell geometries and structures is needed to objectively evaluate the potential mitigation of thermal runaway, especially in the absence of the Al PCC.

Post-mortem X-ray CT

The three-dimensional (3D) reconstructions from post-mortem CT scans of the G3 cells (Al PCC + Cu PCC) are shown in Figure 4 and were used to validate the hypotheses deduced from the radiographs in Figure 3. The cathode is represented by the thicker bright gray layers due to the high level of X-ray attenuation. The thin dark line in the middle of the layers is the Al film-coated PCC, as the polymer and Al film coated on the PCC have much lower attenuation. Graphite also has relatively low attenuation and is shown by the thicker dark gray layers.

Figure 4A highlights the flexibility of the PCC electrode assembly to accept the mechanical deformation from the nail penetration. In addition, the preventive mechanism in Al PCC cells occurred before the compromise of the safety components, as the current interrupt device (CID), the CID vent, and the PTC device remained intact. These safety measures specific to the cylindrical cell format (e.g., 18650, 21700, 26650) at the cell-casing level, highlight the rapid preventive response of

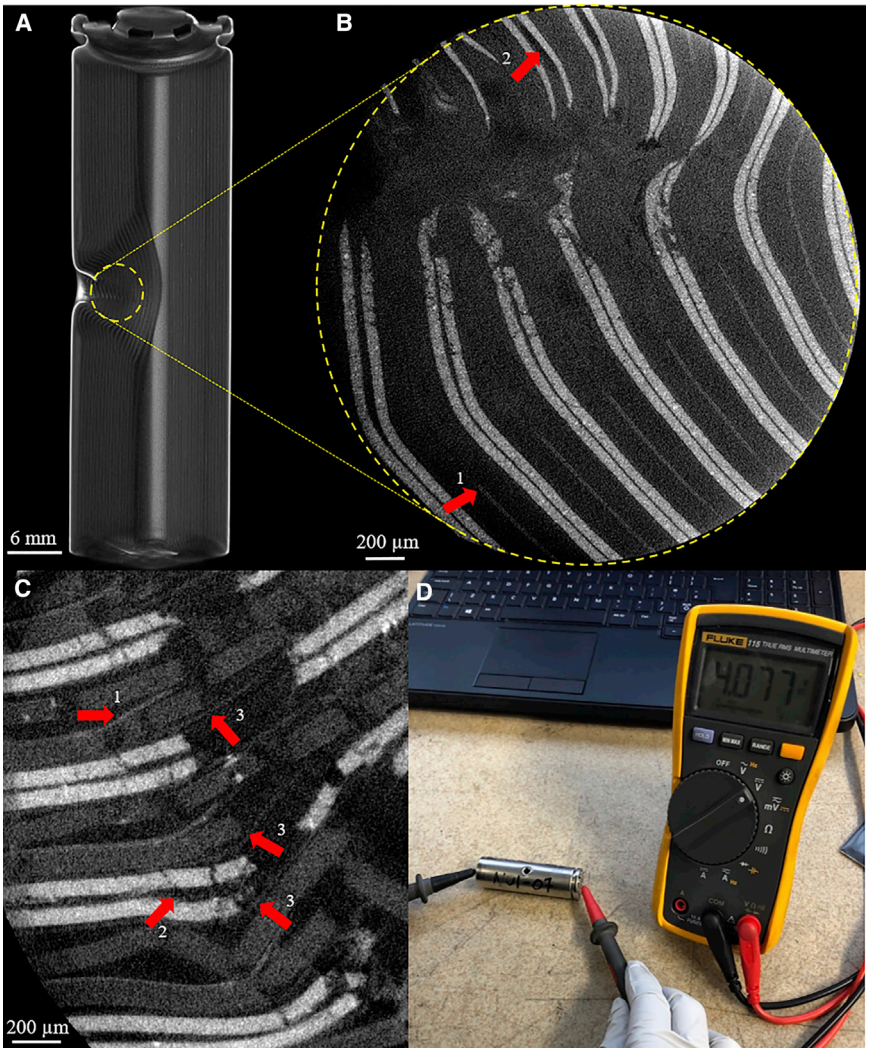

Figure 4. Post-mortem analysis of G3 cells

Numbered arrows represent the same feature observed across multiple locations and are not limited to the examples marked, in which 1 indicates the negative Cu PCC, 2 highlights the positive Al PCC, and 3 shows the separator.

(A) Reconstructed tomogram of the entire nail-penetrated cell (G3-02, Al PCC + Cu PCC), showing evidence of the shear forces exerted on the electrode assembly.

(B) Cylindrical cross-section of the nail penetration path shown in (A) of cell G3-02 (Al PCC + Cu PCC), providing visualization of the structure and indicators of the phenomena that occurred during mechanical abuse.

(C) Cylindrical cross-section ortho-slice of the nail penetration path in the penetrated direction for cell G3-03 (Al PCC + Cu PCC). This interior-focused field of view provided visualization of the internal structure after nail penetration at 1.76 µm pixel size.

(D) Post-nail-penetration test OCV measurement showed 4.077 V for cell G1-01.

the PCC local to the region of short circuit at the electrode level. Consequently, it can be inferred that the cell-level safety devices common to most cylindrical cell formats (e.g., PTCs) did not respond sufficiently fast to the internal short circuit via the nail. This highlights the significance in preventing the development of microscopic failures into cell-level thermal runaway. Fractured electrodes can be observed along the nail-penetration path, which were subsequently investigated using region of interest (ROI) CT as displayed in Figure 4B. The ROI X-ray CT was acquired with a 1.76 µm pixel resolution, which was sufficient to resolve both the polymer and the metal coating of the PCC and to deduce the sequence of events during nail penetration.

CellPress
OPEN ACCESS

Both PCCs were visible in the ortho-slices (Figures 4B and 4C), and the Al PCC and Cu PCC were observed to have shrunk away from the region of elevated temperature around the path of the nail, as indicated by arrow 1 and 2, respectively, in both Figures 4B and 4C. In regions where the PCC had withdrawn from the elevated temperature region, a black void is visible, indicating the complete absence of the PCC, as highlighted, for example, by arrow 2 in Figure 4B. The lack of PCC to bind the double electrode layer together caused the double anode and cathode layers to split apart. These findings reaffirm the observations of the *operando* radiography.

Higher-resolution imaging focused on the damaged electrode layers adjacent to the nail, as shown in Figure 4C for cell G3-03. Material was visible between the cathode and anode at a similar attenuation level to the polymer core of the PCC, indicated by arrow 3. This material was determined to be the separator, which had maintained its integrity and was still found between the anode and cathode, despite the fact that adjacent PCCs on either side had melted or shrunk away from the path of the nail. This is significant, as it provides further evidence that the PCC thermal degradation shrinking safety mechanism operated as expected, deploying before any separator failure, and isolated the cathode sufficiently to prevent further short circuiting leading to thermal runaway.

DISCUSSION

Multi-length scale analysis with high-speed X-ray radiography and post-mortem CT, combined with fractional thermal runaway calorimetry, provided a detailed comparison between the thermal runaway mechanism during nail penetration of PCC cells and that of standard commercial CC cells. The mechanical abuse tests conducted provide evidence that the Al PCC demonstrated the complete prevention of thermal runaway in an 18650 geometry cell with Li-ion nickel-manganese-cobalt (NMC) cathode and graphite anode. In both Al and Cu PCCs, shrinkage of the core polymer layer from the interface between nail and electrode assembly caused the anode and cathode layers to split apart due to a lack of bonding with the PCC. The absence of the PCC in close proximity to the elevated temperature nail-penetrated path in high-resolution X-ray CT, coupled with the intact separator, provides solid evidence for the hypothesized shrinking safety mechanism of the Al PCC.

Cells with the Al PCC showed potential for functionality after nail penetration, as the cells held voltage above 3.60 V for 8 months. The Cu PCC by itself is insufficient to prevent thermal runaway during this method of mechanical abuse. This is attributed to the nail bridging the electrically negative can, which is connected to the graphite anode, with the Al CC and the cathode. Therefore, despite the protection offered to the graphite local to the nail, the Al CC offered no additional protection to the cathode, and this resulted in thermal runaway. However, further testing would be required with different format cells where the cell casing is not electrically conductive to provide an unbiased evaluation of the Cu PCC. This would be possible in pouch or prismatic cells where the cell casing is not electrically connected to either of the electrodes and the Cu PCC could isolate the negative electrode from the positive electrode. Adoption of the Al PCC in pouch cells would provide a thermal runaway contingency, which would contribute immensely to reducing the consequences of failure in a cell geometry with much fewer safety components than an 18650 cell.

The results presented here demonstrate a great advance in improving the safety of Li-ion batteries, while also reducing cost and increasing the energy density of cells

when scaled to manufacturing commercial cell formats as well as at the module level. Typically, efforts into the advancement of battery safety to ensure commercial adaptation is driven by the development of new materials. Examples include new electrodes and non-flammable electrolytes, the adoption of which requires time-intensive, multivariate, and experimental optimization of these novel components. The innovative structure provided by the PCC architecture offers the safety advances reported in this work, which is independent of cell chemistry (provided the PCC is stable in the operating environment). Moreover, the properties of the PCC allow for assimilation with current cylindrical cell roll-to-roll manufacturing technology.

The promise shown by the PCC in prevention and potential for mitigation presents the scope for future work towards other failure mechanisms such as thermal and internal short circuit abuse. We acknowledge that only 10 tests were conducted in total for this work, and therefore we cannot say with statistical confidence that this material will withstand nail-penetration thermal runaway 100% of the time, but this work nonetheless demonstrates a substantial improvement in safety, with 6 out of 6 successful demonstrations with the Al PCC, where otherwise thermal runaway would certainly occur.

EXPERIMENTAL PROCEDURES

Resource availability

Lead contact

Further information and request for resources should be directed to and will be fulfilled by the lead contacts, Donal P. Finegan (donal.finegan@nrel.gov.) and Paul R. Shearing (p.shearing@ucl.ac.uk).

Materials availability

This study did not generate new unique reagents.

Data and code availability

The high-speed X-ray radiography data generated during this study are available as videos in the Supplemental Information. All other data are available from the authors upon reasonable request.

Experimental methods

Cells were manufactured with both commercial CCs and their PCC counterparts; comparative material properties and thicknesses are shown in Figure S1. Nail penetration and PCC evaluation were investigated by *operando* X-ray imaging, post-mortem X-ray micro-CT, and thermal statistical analysis to understand the internal phenomena and external thermal response. In all of the tests conducted, the internal CC tabs were avoided during nail penetration, guided by *a priori* tomogram acquisition (Figure 1C). Penetration of the negative tab welded to the cell casing would not have affected the outcome as the Al PCC would have protected the cathode layers. However, nail penetration of the positive tab in the electrode assembly would cause the cell to fail as there is no Al PCC present to protect this tab; however, doing so would not provide evaluation of the Al PCC, and hence the internally welded tabs were avoided.

Four configurations of cells (G1, G2, G3, and G4) with different CCs that were tested are shown in Figure 1C. A combination of the standard metal CCs (Al CC, Cu CC), the polymer Al CC (Al PCC), the polymer Cu CC (Cu PCC), and both polymer Al and Cu CCs (Al + Cu PCC) were used in non-bottom vent and otherwise identical 18650 cells. The PCC materials were manufactured and

CellPress
OPEN ACCESS

provided by the Soteria Battery Innovation Group (Greenville, SC, USA). Li-ion 18650 cells consisting of $LiNi_{0.5}Mn_{0.3}Co_{0.2}O_2$ (NMC-532) and graphite electrodes were used in this work and were custom manufactured by Coulometrics (Chattanooga, TN, USA). Multiple abuse tests were conducted to ensure the repeatability of results. Cells were rated at 2.10 Ah capacity at 0.20 C and were charged using a constant current-constant voltage (CC-CV) protocol. Cells were charged to 4.20 V at 0.50 C constant current and then held at constant voltage until the current was <0.02 C before abuse testing. Cells were tested at 4.20 V to provide the worst-case scenario outcome should it occur, as well as increase the likelihood for a micro-short circuit to initiate and develop into a macro-short circuit whereby the heat generation from thermal decomposition propagates cell-level thermal runaway.

The effectiveness of the safety mechanism of the PCC is predicated on whether it deploys before separator failure, as shown in Figure 1B. Thus, to investigate the most challenging environment for the PCC to function, a 10 μm-thick single-layer polypropylene separator was used. For comparison, typical commercial separators are usually <25 μm thick[41–44] and are single-layer, tri-layer, or ceramic-coated polyolefin separators; therefore, in most cases they would likely be more thermally stable than a 10 μm-thick single-layer polypropylene separator.

X-ray radiography

High-speed X-ray imaging at 2,000 frames per second was performed at beamline ID19 at the European Synchrotron Radiation Facility (ESRF) to capture the internal dynamic structural phenomena during testing. The cells were imaged under a polychromatic beam with a pixel size of 10.00 μm and a 2,016 × 1,111-pixel (horizontal × vertical) field of view (FOV). A PCO.Dimax (PCO AG, Kelheim, Germany) detector and a LuAG:Ce ($Lu_3Al_{15}O_{12}$:Ce) scintillator (Crytur, Turnov, Czech Republic) were used for all high-speed imaging experiments. The radiographs were flat-field corrected and enhanced using MATLAB's adaptive histogram equalization (adapthisteq) function.

X-ray micro-CT

Laboratory-based X-ray CT was used to evaluate the safety mechanism of the PCC non-destructively by interior tomography acquisition across multiple length scales. Non-destructive X-ray CT was conducted using laboratory X-ray systems: a Nikon XT H225 (Tokyo, Japan), 225 kV, with a PerkinElmer 1620 Detector (Waltham, MA, USA), and a Zeiss Xradia 520 Versa (Carl Zeiss, Dublin, CA, USA) were used to acquire flat-field-corrected orthogonal radiographs to be reconstructed into 3D volumetric data. Both CT systems use a tungsten target; accelerating voltages and beam powers are shown in Table 1, and were selected based on the attenuation of the samples and the contrast of the component materials to ensure that features of interest were resolvable. The resulting radiographs were reconstructed using commercial software packages (CT Pro 3D and Zeiss XMReconstructor), which use algorithms based on standard filtered back-projection or Feldkamp-Davis-Kress (FDK).

Cells were scanned with an increasingly focused FOV and a greater resolution—from a 35.5 μm pixel size, corresponding to a 70 × 70 mm FOV, to 1.76 × 1.76 μm pixel resolution, and 3.6 × 3.6 mm FOV (imaging configurations are shown in Table 1). The highest resolution interior volumetric data acquisitions were required to provide visualization of the electrode layers post-testing—in particular, the PCC, which surrounded the nail. Tomograms were acquired using the Zeiss Xradia 520 Versa using the "Scout & Zoom" technique.[45–48] This was required to visualize the CC

Table 1. Imaging configurations for lab-based X-ray micro-CT

Technique	Voxel size, μm	Field of view, mm	Accelerating voltage, kV	X-ray tube power, W	Filter	Projections
XRM–Nikon XT 255	35.5	70 × 70	200	35	0.1 mm Cu	1,848
XRM–Nikon XT 255	10.5	20 × 20	200	35	0.1 mm Cu	3,176
XRM–520 Versa (4× magnification)	1.77	3.6 × 3.6	160	10	Zeiss HE3	1,801

Zeiss HE3 filter is a proprietary filter provided by Zeiss as part of the Xradia 520 Versa. XRM, X-ray microscopy.

adequately. An initial coarse scan was conducted to establish the orientation and axes of the sample before a more detailed interior tomography was acquired. Post-reconstruction, visualization of the reconstructed tomograms was processed using Avizo Fire 9.5 software (ThermoFisher Visualization Sciences Group [VSG], Merignac, France).

FTRC

A custom-designed FTRC was used as described in previous work.[18,29] An ambidextrous design accounted for the permutations of failure such as bottom vent cell ejection or spin groove breaches. Figure 5A shows the fully assembled calorimeter enclosed in thermal insulating blocks composed of sealed glass cells (FOAMGLAS, Pittsburgh Corning, Toledo, OH, USA). For this study, the Al calorimeter design allows for X-ray transparency to probe the internal phenomena, nail-penetration functionality, portability, and ability to perform high-throughput failure testing.

An interchangeable Al 18650 cell chamber enclosed the cell, as shown in Figure 5C, capable of testing 18650 format commercial cells with varying chemistries, capacities, and safety mechanisms, such as bottom vents. It is designed to discern the energy from the casing of the cell and the ejected contents; the cell chamber was thermally insulated from the rest of the calorimeter with thermally insulative ceramic.

The nail penetrated to a depth of 9 mm, an event that took ~1.1–1.6 s and was similar to nail penetration in previous studies.[29] The temperature at the tip of the nail was recorded via an additional thermocouple placed inside the hollow shaft of the nail.[26,30] Statistical analysis derived from the thermal runaway temperature data, provided by thermocouples throughout the axial direction, yielded insight into the total thermal runaway calorific output, with the decoupled heat contributions correlated with the cell casing and ejected material.

SUPPLEMENTAL INFORMATION

Supplemental Information can be found online at https://doi.org/10.1016/j.xcrp.2021.100360.

ACKNOWLEDGMENTS

The authors would like to acknowledge the expertise provided by Zoran Bilc and Erman Cihan during the calorimeter design, assembly, and instrumentation. Special thanks to the supporting facilities and technical staff at the NASA JSC Energy Systems and Test Area (ESTA). We are grateful for the provision of synchrotron beamtime by the ESRF on beamline ID19 and for allowing us to use their facilities (Experiment ME 1515). The authors would like to acknowledge the EPSRC for supporting the energy storage work in the Electrochemical Innovation Lab (EP/R020973/1; EP/R023581/1; EP/N032888/1; EP/N001583/1; EP/P009050/1; EP/M009394/1; EP/M014371/1). This work was partly funded by the National Measurement System

CellPress
OPEN ACCESS

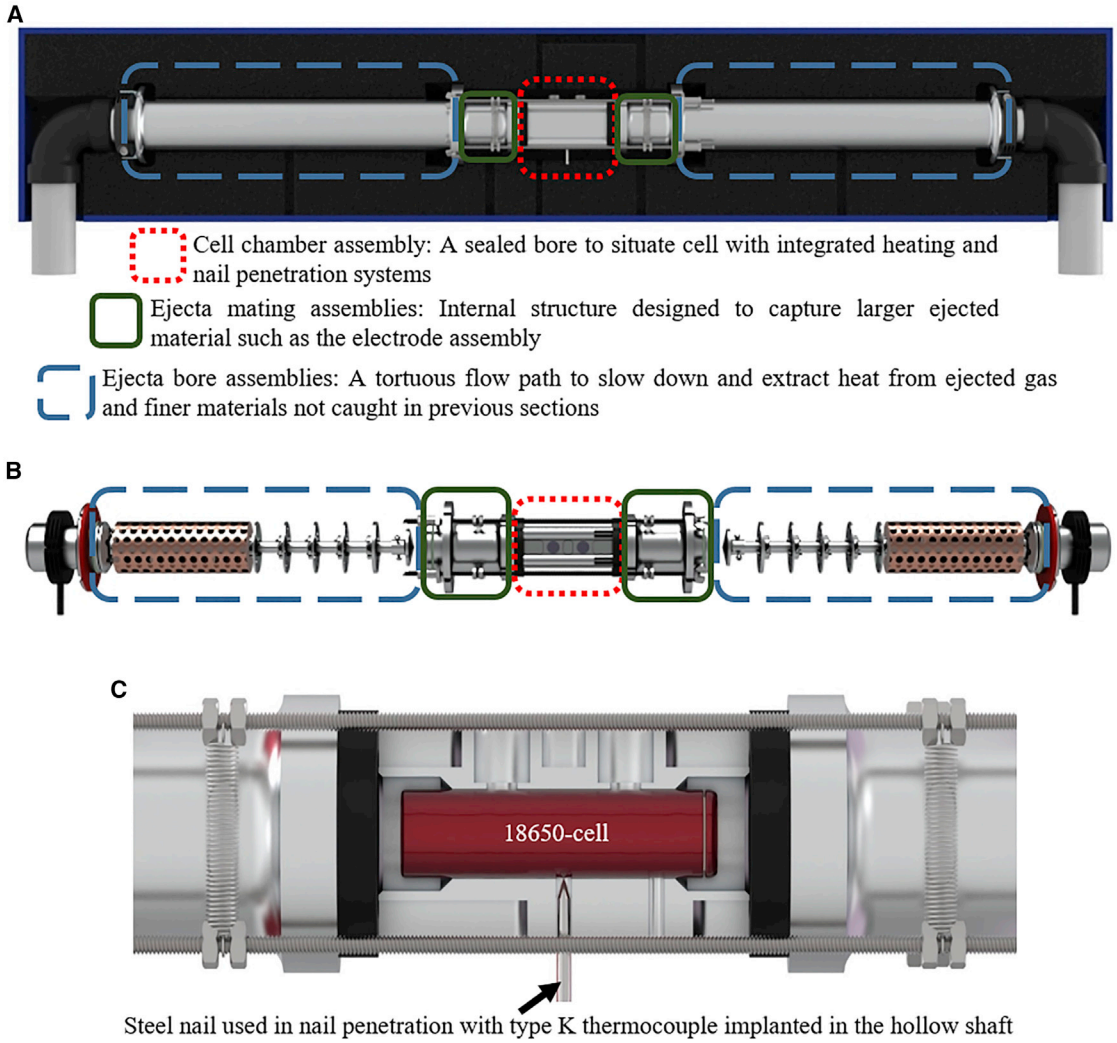

Figure 5. Calorimeter and nail penetration cell chamber

(A) Rendering of the fully assembled calorimeter inside a thermally insulating calorimeter casing.

(B) A magnified view of the FTRC internal structure.

(C) Rendering of the Al nail penetration cell chamber using a steel nail with an internal thermocouple. Additional features include spring pressurized cell skin thermocouples, gas sealing O-rings, and thermally isolating ceramic.

of the UK Department of Business, Energy, and Industrial Strategy. The authors would also like to acknowledge the Royal Academy of Engineering for funding P.R.S. through CiET1718/59 and the Faraday Institution (EP/S003053/1, FIRG001). The authors also acknowledge the STFC for supporting P.R.S. and D.J.L.B. and for an Experiment Design Award for M.T.M.P under the auspices of the STFC Batteries Network (ST/R006873/1). This work was authored in part by the National Renewable Energy Laboratory, operated by Alliance for Sustainable Energy, LLC, for the US Department of Energy (DOE) under contract no. DE-AC36-08GO28308. Funding was provided by the US DOE Office of Energy Efficiency and Renewable Energy Vehicle Technologies Office. The views expressed in the article do not necessarily represent the views of the DOE or the US government. The US government retains and the publisher, by accepting the article for publication, acknowledges that the US government retains a nonexclusive, paid-up, irrevocable, worldwide license to

publish or reproduce the published form of this work, or allow others to do so, for US government purposes.

AUTHOR CONTRIBUTIONS

Conceptualization, E.D., D.P.F., and P.R.S.; methodology, M.T.M.P., J.J.D., W.Q.W., and D.P.F.; investigation, M.T.M.P., J.J.D., T.M.M.H., D.P., F.I., A.R., M.P.O., and D.P.F.; formal analysis, M.T.M.P., W.Q.W., F.I., A.R., M.P.O., and D.P.F.; resources, A.R., M.P.O., E.D., and P.R.S.; writing – original draft, M.T.M.P.; writing – review & editing, T.M.M.H., A.R., G.H., D.J.L.B., E.D., D.P.F., and P.R.S.; visualization, M.T.M.P., D.P., F.I., and D.P.F.; supervision, G.H., D.J.L.B., E.D., and P.R.S.

DECLARATION OF INTERESTS

The authors declare no competing interests.

Received: September 11, 2020
Revised: January 6, 2021
Accepted: February 15, 2021
Published: March 19, 2021

REFERENCES

1. Zaghib, K., Dontigny, M., Guerfi, A., Charest, P., Rodrigues, I., Mauger, A., and Julien, C.M. (2011). Safe and fast-charging Li-ion battery with long shelf life for power applications. J. Power Sources *196*, 3949–3954.
2. Fan, J. (2004). Studies of 18650 cylindrical cells made with doped linio2 positive electrodes for military applications. J. Power Sources *138*, 288–293.
3. Larcher, D., and Tarascon, J.M. (2015). Towards greener and more sustainable batteries for electrical energy storage. Nat. Chem. *7*, 19–29.
4. Feng, X., Ouyang, M., Liu, X., Lu, L., Xia, Y., and He, X. (2018). Thermal runaway mechanism of lithium ion battery for electric vehicles: a review. Energy Storage Mater. *10*, 246–267.
5. Williard, N., He, W., Hendricks, C., and Pecht, M. (2013). Lessons learned from the 787 dreamliner issue on lithium-ion battery reliability. Energies *6*, 4682–4695.
6. Liu, B., Jia, Y., Yuan, C., Wang, L., Gao, X., Yin, S., and Xu, J. (2020). Safety issues and mechanisms of lithium-ion battery cell upon mechanical abusive loading: a review. Energy Storage Mater. *24*, 85–112.
7. Lu, L.L., Ge, J., Yang, J.N., Chen, S.M., Yao, H.B., Zhou, F., and Yu, S.H. (2016). Free-standing copper nanowire network current collector for improving lithium anode performance. Nano Lett. *16*, 4431–4437.
8. Myung, S.T., Hitoshi, Y., and Sun, Y.K. (2011). Electrochemical behavior and passivation of current collectors in lithium-ion batteries. J. Mater. Chem. *21*, 9891–9911.
9. Chen, Z., Qin, Y., Ren, Y., Lu, W., Orendorff, C., Roth, E.P., and Amine, K. (2011). Multi-scale study of thermal stability of lithiated graphite. Energy Environ. Sci. *4*, 4023–4030.
10. Lopez, C.F., Jeevarajan, J.A., and Mukherjee, P.P. (2015). Experimental Analysis of Thermal Runaway and Propagation in Lithium-Ion Battery Modules. J. Electrochem. Soc. *162*, A1905–A1915.
11. Feng, X., Fang, M., He, X., Ouyang, M., Lu, L., Wang, H., and Zhang, M. (2014). Thermal runaway features of large format prismatic lithium ion battery using extended volume accelerating rate calorimetry. J. Power Sources *255*, 294–301.
12. Zheng, S., Wang, L., Feng, X., and He, X. (2018). Probing the heat sources during thermal runaway process by thermal analysis of different battery chemistries. J. Power Sources *378*, 527–536.
13. Fu, Y., Lu, S., Li, K., Liu, C., Cheng, X., and Zhang, H. (2015). An experimental study on burning behaviors of 18650 lithium ion batteries using a cone calorimeter. J. Power Sources *273*, 216–222.
14. Wang, Q., Ping, P., Zhao, X., Chu, G., Sun, J., and Chen, C. (2012). Thermal runaway caused fire and explosion of lithium ion battery. J. Power Sources *208*, 210–224.
15. Bandhauer, T.M., Garimella, S., and Fuller, T.F. (2011). A Critical Review of Thermal Issues in Lithium-Ion Batteries. J. Electrochem. Soc. *158*, R1.
16. Spotnitz, R., and Franklin, J. (2003). Abuse behavior of high-power, lithium-ion cells. J. Power Sources *113*, 81–100.
17. Pham, M.T.M., Darst, J.J., Finegan, D.P., Robinson, J.B., Heenan, T.M.M., Kok, M.D.R., Iacoviello, F., Owen, R., Walker, W.Q., Magdysyuk, O.V., et al. (2020). Correlative acoustic time-of-flight spectroscopy and X-ray imaging to investigate gas-induced delamination in lithium-ion pouch cells during thermal runaway. J. Power Sources *470*, 228039.
18. Walker, W.Q., Darst, J.J., Finegan, D.P., Bayles, G.A., Johnson, K.L., Darcy, E., and Rickman, S.L. (2019). Decoupling of heat generated from ejected and non-ejected contents of 18650-format lithium-ion cells using statistical methods. J. Power Sources *415*, 207–218.
19. Robinson, J.B., Darr, J.A., Eastwood, D.S., Hinds, G., Lee, P.D., Shearing, P.R., Taiwo, O.O., and Brett, D.J.L. (2014). Non-uniform temperature distribution in Li-ion batteries during discharge - a combined thermal imaging, X-ray micro-tomography and electrochemical impedance approach. J. Power Sources *252*, 51–57.
20. Hausbrand, R., Cherkashinin, G., Ehrenberg, H., Gröting, M., Albe, K., Hess, C., and Jaegermann, W. (2015). Fundamental degradation mechanisms of layered oxide Li-ion battery cathode materials: methodology, insights and novel approaches. Mater. Sci. Eng. B *192*, 3–25.
21. Sharma, N., Peterson, V.K., Elcombe, M.M., Avdeev, M., Studer, A.J., Blagojevic, N., Yusoff, R., and Kamarulzaman, N. (2010). Structural changes in a commercial lithium-ion battery during electrochemical cycling: an in situ neutron diffraction study. J. Power Sources *195*, 8258–8266.
22. Waag, W., Käbitz, S., and Sauer, D.U. (2013). Experimental investigation of the lithium-ion battery impedance characteristic at various conditions and aging states and its influence on the application. Appl. Energy *102*, 885–897.
23. Ren, D., Feng, X., Lu, L., Ouyang, M., Zheng, S., Li, J., and He, X. (2017). An electrochemical-thermal coupled overcharge-to-thermal-runaway model for lithium ion battery. J. Power Sources *364*, 328–340.

CellPress
OPEN ACCESS

24. Yokoshima, T., Mukoyama, D., Maeda, F., Osaka, T., Takazawa, K., Egusa, S., Naoi, S., Ishikura, S., and Yamamoto, K. (2018). Direct observation of internal state of thermal runaway in lithium ion battery during nail-penetration test. J. Power Sources *393*, 67–74.

25. Yokoshima, T., Mukoyama, D., Maeda, F., Osaka, T., Takazawa, K., and Egusa, S. (2019). Operando analysis of thermal runaway in lithium ion battery during nail-penetration test using an X-ray inspection system. J. Electrochem. Soc. *166*, A1243–A1250.

26. Finegan, D.P., Tjaden, B., Heenan, M.M., Jervis, T., Michiel, R., Di, M., Rack, A., Hinds, G., Brett, D.J.L., and Shearing, P.R. (2017). Tracking Internal Temperature and Structural Dynamics during Nail Penetration of Lithium-Ion Cells. J. Electrochem. Soc. *164*, A3285–A3291.

27. Finegan, D.P., Scheel, M., Robinson, J.B., Tjaden, B., Hunt, I., Mason, T.J., Millichamp, J., Di Michiel, M., Offer, G.J., Hinds, G., et al. (2015). In-operando high-speed tomography of lithium-ion batteries during thermal runaway. Nat. Commun. *6*, 6924.

28. Finegan, D.P., Darcy, E., Keyser, M., Tjaden, B., Heenan, T.M.M., Jervis, R., Bailey, J.J., Malik, R., Vo, N.T., Magdysyuk, O.V., et al. (2017). Characterising thermal runaway within lithium-ion cells by inducing and monitoring internal short circuits. Energy Environ. Sci. *10*, 1377–1388.

29. Finegan, D.P., Darst, J., Walker, W., Li, Q., Yang, C., Jervis, R., Heenan, T.M.M., Hack, J., Thomas, J.C., Rack, A., et al. (2019). Modelling and experiments to identify high-risk failure scenarios for testing the safety of lithium-ion cells. J. Power Sources *417*, 29–41.

30. Hatchard, T.D., Trussler, S., and Dahn, J.R. (2014). Building a "smart nail" for penetration tests on Li-ion cells. J. Power Sources *247*, 821–823.

31. Ci, S., Lin, N., and Wu, D. (2016). Reconfigurable Battery Techniques and Systems: A Survey. IEEE Access *4*, 1175–1189.

32. Hendricks, C., Williard, N., Mathew, S., and Pecht, M. (2015). A failure modes, mechanisms, and effects analysis (FMMEA) of lithium-ion batteries. J. Power Sources *297*, 113–120.

33. Liao, Z., Zhang, S., Li, K., Zhang, G., and Habetler, T.G. (2019). A survey of methods for monitoring and detecting thermal runaway of lithium-ion batteries. J. Power Sources *436*, 226879.

34. Spielbauer, M., Berg, P., Ringat, M., Bohlen, O., and Jossen, A. (2019). Experimental study of the impedance behavior of 18650 lithium-ion battery cells under deforming mechanical abuse. J. Energy Storage *26*, 101039.

35. Chiu, K.C., Lin, C.H., Yeh, S.F., Lin, Y.H., and Chen, K.C. (2014). An electrochemical modeling of lithium-ion battery nail penetration. J. Power Sources *251*, 254–263.

36. Lamb, J., and Orendorff, C.J. (2014). Evaluation of mechanical abuse techniques in lithium ion batteries. J. Power Sources *247*, 189–196.

37. Mao, B., Chen, H., Cui, Z., Wu, T., and Wang, Q. (2018). Failure mechanism of the lithium ion battery during nail penetration. Int. J. Heat Mass Transf. *122*, 1103–1115.

38. Naguib, M., Allu, S., Simunovic, S., Li, J., Wang, H., and Dudney, N.J. (2018). Limiting Internal Short-Circuit Damage by Electrode Partition for Impact-Tolerant Li-Ion Batteries. Joule *2*, 155–167.

39. Liu, S., Trela, J.A., and Karimi, K.J. (2017). Battery cell design for preventing internal short circuits from occurring and propagating using positive temperature coefficient (PTC) materials, US patent US2018/0269535A1, filed July 12, 2017, and granted May 12, 2020.

40. Finegan, D.P., Scheel, M., Robinson, J.B., Tjaden, B., Di Michiel, M., Hinds, G., Brett, D.J.L., and Shearing, P.R. (2016). Investigating lithium-ion battery materials during overcharge-induced thermal runaway: an operando and multi-scale X-ray CT study. Phys. Chem. Chem. Phys. *18*, 30912–30919.

41. Li, Y., and Pu, H. (2018). Facile fabrication of multilayer separators for lithium-ion battery via multilayer coextrusion and thermal induced phase separation. J. Power Sources *384*, 408–416.

42. Zhang, S.S. (2007). A review on the separators of liquid electrolyte Li-ion batteries. J. Power Sources *164*, 351–364.

43. Lee, H., Yanilmaz, M., Toprakci, O., Fu, K., and Zhang, X. (2014). A review of recent developments in membrane separators for rechargeable lithium-ion batteries. Energy Environ. Sci. *7*, 3857–3886.

44. Lagadec, M.F., Zahn, R., and Wood, V. (2019). Characterization and performance evaluation of lithium-ion battery separators. Nat. Energy *4*, 16–25.

45. Gelb, J., Finegan, D.P., Brett, D.J.L., and Shearing, P.R. (2017). Multi-scale 3D investigations of a commercial 18650 Li-ion battery with correlative electron- and X-ray microscopy. J. Power Sources *357*, 77–86.

46. Merkle, A.P., and Gelb, J. (2013). The Ascent of 3D X-ray Microscopy in the Laboratory. Micros. Today *21*, 10–15.

47. Feser, M., Gelb, J., Chang, H., Cui, H., Duewer, F., Lau, S.H., Tkachuk, A., and Yun, W. (2008). Sub-micron resolution CT for failure analysis and process development. Meas. Sci. Technol. *19*, 094001.

48. Burnett, T.L., McDonald, S.A., Gholinia, A., Geurts, R., Janus, M., Slater, T., Haigh, S.J., Ornek, C., Almuaili, F., Engelberg, D.L., et al. (2014). Correlative tomography. Sci. Rep. *4*, 4711.